Journal of Power Sources 633 (2025) 236390

Contents lists available at ScienceDirect

Journal of Power Sources

journal homepage: www.elsevier.com/locate/jpowsour

The utilization of high saline sodium chloride containing waters in solid oxide electrolysers

Jan Uecker [a,b], Lucy Nohl [a], Vaibhav Vibhu [a,*], Jean-Pierre Poc [a,b], Pritam Chakraborty [a,b], Izaak C. Vinke [a], Shibabrata Basak [a], L.G.J.(Bert) de Haart [a], Rüdiger-A. Eichel [a,b]

[a] Institute of Energy Technologies, Fundamental Electrochemistry (IET-1), Forschungszentrum Jülich GmbH, 52425, Jülich, Germany
[b] Institute of Physical Chemistry, RWTH Aachen University, 52074, Aachen, Germany

HIGHLIGHTS

- Initial performance is not influenced using NaCl containing water.
- Salt is transported to the cell during operation.
- Using NaCl containing solutions accelerate degradation.
- Direct utilization of NaCl containing water in SOECs is not recommended.

ARTICLE INFO

Keywords:
SOECs
Wastewater
Saltwater
Seawater
Electrochemical performance
Stability
Degradation

ABSTRACT

State-of-the-art electrolyser systems are based on the utilization of highly pure freshwater. This could lead to an increase in freshwater demand and a worsening of freshwater water scarcity. One solution is the direct use of saline waters such as seawater or wastewaters from industry. In this work, the impact of sodium chloride contamination in waters on high temperature solid oxide electrolysis cells is investigated. Thus, the utilization of high saline wastewater from industry and an accelerated stress test for the use of seawater in SOECs is evaluated. The initial performance and stability are compared with results gathered by utilizing high-purity freshwater for steam generation. An increased degradation rate was observed for the sodium chloride solution after 400 h of operation. The increased degradation is mainly caused by an accelerated increase in ohmic and polarisation resistance. More specifically, the charge transfer process in the Ni-YSZ fuel electrode was found to contribute significantly to the increased degradation. Post-test characterization using XPS and SEM-EDX showed sodium particle deposition on the fuel electrode surface contact layer confirming the transport of salt to the cell. The cross-section analysis by SEM showed an accelerated Ni agglomeration in the Ni-YSZ fuel electrode compared to pure water operation.

1. Introduction

In the current decade, the water demand increased continuously every year and is expected to increase further due to the growing population, rising incomes and expanding cities [1,2]. On the other hand, water supply is becoming more erratic and uncertain which will lead to higher water scarcity and water stress [1]. For instance, it is predicted that the global urban population that faces water scarcity will increase from 933 million people (1/3 of the global urban population) in 2016 to 1.7–2.4 billion (nearly half of the global urban population) in 2050 [3]. Economically speaking water scarcity impacts agriculture, health and incomes all over the world and could negatively impact the Gross Domestic Product (GDP) of some regions by about 6 % which leads to poverty and conflicts [4]. Another factor which exacerbates water scarcity is climate change due to global warming and extreme weather events [1,4–6]. Thus, in regions such as Central Africa, East Asia and parts of South America where water is currently abundant it will become increasingly scarce and water scarcity will worsen in regions with

* Corresponding author.
E-mail address: v.vibhu@fz-juelich.de (V. Vibhu).

https://doi.org/10.1016/j.jpowsour.2025.236390
Received 29 October 2024; Received in revised form 20 January 2025; Accepted 26 January 2025
Available online 8 February 2025

already low water supply such as the Middle East and several regions in Africa [1]. To prevent further water scarcity and other consequences humankind tries to tackle climate change and keep global warming under 1.5 °C [6]. One key point is the use of renewably generated energy such as solar and wind power where solar radiation has the highest potential in terms of renewable power generation [7]. However, both sources are intermittent and thus favourable inexpensive energy storage and conversion systems are needed. Hydrogen is a promising fuel for chemical energy storage and transportation due to its gravimetric energy density [7]. For the utilization of green hydrogen, huge amounts of freshwater with high purity are necessary with state-of-the-art electrolyser systems. For instance, the demanded amount of green hydrogen in Germany for the year 2050 is predicted to be around 600 TWh/year which is equal to a water consumption of 3300 m^3/s in water electrolyser systems [8,9]. In comparison, private households are consuming around 116 m^3/s freshwater in Germany nowadays [10]. Considering the global irradiation potential is the highest in Africa, South America and Australia these spots are suggested for production plants of hydrogen or other hydrogen-based energy carriers [4,11]. At most of these spots, freshwater scarcity is expected to rise and could be exacerbated by the employing of electrolyser systems [1,4]. This could lead to a competition between economic water usage and water to meet the demands of the local population. One solution would be the desalination and purification of seawater or other wastewater feeding into an electrolyser system. However, desalination and purification of water create highly concentrated waste brine (wastewater) which causes negative impacts on the environment being fed back into the oceans [12–15]. Further issues are the emissions of pollutants and the energy demand of the desalination and purification processes [13,14]. Thus, for minimization of costs and environmental impact the direct use of seawater was discussed in recent years in literature for different electrolyser systems [16–22]. Another approach would be the direct utilization of wastewaters from industry and chemical plants which additionally could enable a closed material cycle and a minimization of costs for recycling. For instance, there are numerous chemical industries in the chlorine sector that produce wastewater with a high content of sodium chloride (10–22 wt %). Two known processes are the synthesis of epoxy-diane resins and epichlorohydrin [23]. Other processes are the synthesis of polycarbonate [24] and the recovery process for lead-acid batteries [25]. Even in the food industry, there are high sodium chloride concentrations in wastewater for example from meat curing, vegetable pickling and fish processing [26]. Thus, the option of direct utilization of wastewater from industry should be investigated.

One promising electrolysis system is solid oxide electrolysis cells (SOECs) which are operated at high temperatures between 700 °C and 900 °C. Due to the high operating temperature, steam is used as an educt for the water splitting reaction in opposition to nongaseous water for room temperature electrolysis systems. The required steam can be directly generated from the wastewater utilizing in the best scenario the waste heat from an industrial plant. Furthermore, in comparison with other electrolyser systems, the SOEC electrolyser possesses favourable thermodynamics and enhanced kinetics. However, research on the utilization of contaminated or not highly pure water in SOECs is still scarce in the literature. Three studies investigated the effect of direct seawater utilization found that there is no impact on the initial performance and degradation behaviour of the SOEC [20,27,28]. However, for higher saline concentrated waters as often seen in wastewater from industrial use, no studies are present to the author's best knowledge. Furthermore, the utilization of high saline water for steam generation could provide information in terms of an accelerated stress test/degradation test for seawater usage.

Therefore, in this work, we have tested the impacts of steam produced from saturated sodium chloride solution on commercial Ni-YSZ based state-of-the-art SOECs. The SOECs were characterized by electrochemical impedance spectroscopy (EIS), distribution of relaxation time (DRT) analysis, current density-voltage characteristics (iV curves) and a long-term stability test over 1000 h. The gathered results are compared to the electrolysis operation with steam generated from pure water in the same test setup. The degraded cells were post-characterized to investigate possible salt deposition on the cell's surface and in the cross-section.

2. Experimental

2.1. Electrochemical measurements

Electrochemical experiments were performed with commercially available fuel electrode supported single cells (Ni-YSZ/YSZ/GDC/LSC) by the company Elcogen with a thickness amounted to 315 ± 35 μm, a diameter of 20 mm and an active area of 0.785 cm^2. Additionally, a thin Ni current collecting layer is found on the porous Ni-YSZ fuel electrode. Further information is given in Ref. [29]. The single cells were mounted in a full ceramic housing in a two-electrode (four-wire) NorEcs Probostat setup by Norwegian Electro Ceramics® (NORECS, Oslo, Norway) [30]. For the separation of the gas compartments at the air and fuel electrode sides, a gold ring was used. The cells were contacted by a nickel mesh at the Ni-YSZ fuel electrode and a platinum current collector at the LSC air electrode. The gas flow at each electrode was controlled by mass flow controllers (MCF, Bronkhorst Nord®, Kamen, Germany) with a flow rate of 9 normal $l \cdot h^{-1}$ at both electrodes. Humidification at the fuel electrode was supplied by leading the H_2 gas flow through a heated water bubbler and consecutive to the fuel electrode gas compartment. The steam content was set to a certain value based on the temperature dependency of the gas vapour. The cells were heated up in pure N_2 atmosphere at the fuel electrode and air at the oxygen electrode to 900 °C with a heating rate of 1.5 °C•min^{-1}. Before electrochemical measurements, the cells were reduced stepwise in hydrogen gas which was balanced with N_2 (Table S1, Supporting information). The electrochemical AC- and DC-measurements were recorded using a Vertex.5A potentiostat/galvanostat with an integrated frequency response analyser module from Ivium Technologies® (Eindhoven, The Netherlands). The iV curves were recorded starting from OCV to 0.6 V then to 1.4 V and back to OCV with a scan rate of 10 mV•s^{-1} monitoring the current response. The EIS data sets were recorded at OCV and from 0.7 V to 1.4 V with an increase of 0.05 V under potentiostatic control with 20 mV ac amplitude in a frequency range from 0.11 Hz to 110 kHz with 21 data points per frequency decade. During the investigations the temperature and gas contents at the fuel electrode were varied and iV curves and EIS data were recorded. The analysis of the EIS data was varied using the commercial RelaxIS® software from RHD-Instruments including DRT analysis and equivalent circuit model (ECM) fitting. The DRT was calculated using the RelaxIS® software by Gaussian discretization. However, as transforming an impedance into a DRT is an 'ill-posed inverse problem' caution must be taken with its interpretation [31]. An evaluation of the trustworthiness of the used DRTs is shown in Fig. S9 in the supporting information. The ohmic resistance (R_Ω), the polarisation resistance (R_p) and the area specific resistance (ASR) were derived from the EIS data. The long term tests were performed under a constant current load of -1 A•cm^{-2}. In between the long-term test was interrupted and iV curves and EIS measurements were performed. A cell was tested with pure water for steam generation as a reference. Thus, in total two cells one operated in pure water and one in NaCl solution were tested and compared in this manuscript. Data visualization was done using the Origin® software package.

2.2. Post-test characterization

2.2.1. XRD

The cells were post-characterized by X-ray diffraction (XRD) at room temperature using a PANanalytical X'pert MPD diffractometer with Mo-Kα incident radiation which was later converted to Cu-Kα to enable better comparison with literature results. The system was operated in a

reflection-transmission spinner configuration with a generator voltage of 55 kV and a tube current of 40 mA.

2.2.2. GI-XRD

The cells were post-characterized by glancing incidence X-ray diffraction (Gi-XRD) at room temperature using a PANanalytical X'pert MPD diffractometer with Cu-Kα incident radiation. The system was operated in a reflection-transmission spinner configuration with a generator voltage of 40 kV and a tube current of 40 mA.

2.2.3. XPS

XPS measurements were performed on the Ni-YSZ surface of the degraded cells. A Phi5000 VersaProbe II (ULVAC-Phi Inc., USA) was used for the measurements. The Source was monochromatic Al Kα (1.486 keV). The X-ray setting was 50 W, 15 kV and 200 μm spot size. The Survey was recorded with 187.5 eV pass energy in 0.8 eV steps and a scanning rate of 100 ms/step. The Quantification of elements was done in at% with Shirley-Background and with empirical relative sensitivity factors.

2.2.4. SEM-EDX

2.2.4.1. Ni-YSZ surface. A plasma-focused ion beam scanning electron microscope (TESCAN Amber X; TESCAN) was used for planar imaging. Secondary electron (SE) imaging was performed using the integrated Everhart-Thornley (E-T) detector and the multidetector (MD), while backscattered electron (BSE) imaging was performed using the MD detector only. A low acceleration voltage of 2 kV was used to enable surface specific resolution. Compositional analysis was performed by energy dispersive X-ray spectroscopy (EDX) using the Elite Super detector from EDAX. Data acquisition and analysis were performed using EDAX Apex Advanced software (version 2.5.1001.0001).

2.2.4.2. Ni-YSZ cross section. A scanning electron microscope (Quanta FEG 650, FEI©) was used for cross-section. A low acceleration voltage of 2 kV was used to enable surface specific resolution. Compositional analysis was performed by energy dispersive X-ray spectroscopy (EDX) using the Elite Super detector from EDAX. Data acquisition and analysis were performed using EDAX Apex Advanced software (version 2.5.1001.0001). The analysis and segmentation of the SEM/EDX images present was done using Python as described in Ref. [32].

3. Results

3.1. Initial performance

The initial performance of a cell operated in steam generated from sodium chloride (NaCl) saturated solution is compared with several cells operated with steam generated from pure water by DC-measurements. In Fig. 1a the iV curves of cells are compared for a gas composition of 60 % H_2O + 40 % H_2 at 800 °C. Steam generated from saturated NaCl seems not to significantly affect the shape of the iV curve or current density values of the SOECs cell. Both cells show a similar current density of around 2.35 A•cm^{-2} at 1.4 V. The higher slopes at higher

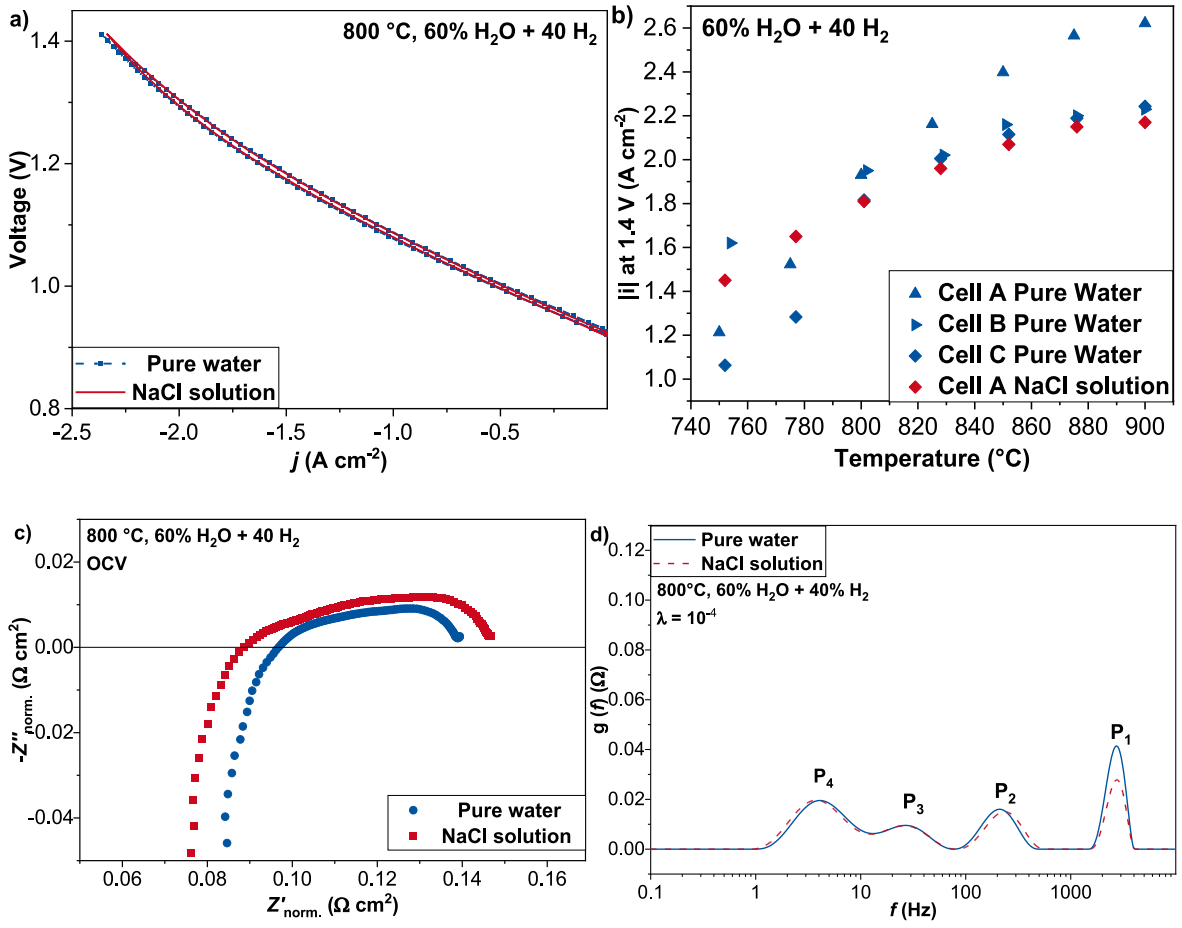

Fig. 1. a) iV curve of commercial Ni-YSZ based SOECs operated in pure water and concentrated sodium chloride solution in 60 % H_2O + 40 % H_2 at 800 °C. b) Current densities at 1.4 V of individual commercial Ni-YSZ based SOECs operated in pure water and saturated sodium chloride solution at various temperatures in 60 % H_2O + 40 % H_2. Corresponding EIS measurements recorded at OCV in the form of c) Nyquist plots and d) DRT comparing the utilization of NaCl solution and pure water for steam generation.

voltage (1.1–1.4 V) can be explained by the mass transport limitations which gain more significance at higher working voltages or currents [33]. In Fig. 1b the current densities at 1.4 V of the NaCl operated cell are compared with various measurements of pure water cells at different temperatures. It is observed that the performance is not significantly influenced which indicates the suitability of utilizing high saline sodium chloride containing wastewaters for SOEC operation in terms of initial performance measures.

Next, AC measurements were performed with the usage of NaCl solution for steam generation and compared with pure water measurements at OCV. In Fig. 1c the Nyquist plots of the NaCl operated cells and a pure water cell operated in a gas composition of 60 % H_2O + 40 % H_2 at 800 °C are shown. From the Nyquist plot, slight differences in the high frequency intercept with the x-axis can be observed comparing both cells. The difference is explained by variations in the electrolyte thickness due to manufacturing and/or slightly different contacting of the cells. The shape of the Nyquist plots looks similar for both cells. The low frequency intercept is slightly higher in value for the NaCl operated cell. This could be explained by measuring two different individual cells or slight variations in operating temperature. Thus, in Fig. S1a in the supporting information, several Nyquist plots of cells operated in pure water and NaCl solution are compared. All cells exhibit slight differences in their shape and intercept values with the *x*-axis which is not casual connected to the utilization of NaCl solution for steam generation.

For further deconvolution of the individual processes, the DRT analysis is performed as shown in Fig. 1d for two explementary cells. Several tested cells and their DRT spectra can be found in Figure SI in the supporting information (Fig. S1b). From the DRT analysis, the following statements are made. Firstly, both pure water and NaCl cells show four peaks (labelled here from P_1 to P_4) suggesting up to four individual time constants. The high frequency peak P_1 overlaps for all measured cells and has a relaxation frequency between 1500 and 4000 Hz. In Fig. 1d the magnitude of P_1 is slightly higher for the pure water cells compared with the NaCl cell. Comparing all measured cells (Fig. S1b) the observed changes in magnitude are not related to the usage of NaCl saturated solution. The peak P_2 is observed in a relaxation frequency range from 100 to 500 Hz and shifts in its relaxation frequency comparing the measurements as seen in Fig. S1b. For the measurements in Fig. 1d, no difference in magnitude or relaxation frequency is observed comparing the pure water and NaCl cells. The peak P_3 exhibits a relaxation frequency of 10–80 Hz. No difference between the pure water and the NaCl solution is seen. Again, in several measurements, the magnitude and specific relaxation frequency are slightly changing as shown in Fig. S1b. However, no relationship to the utilization of NaCl solution is observed. P_4 has the lowest relaxation frequency of 1–10 Hz. In conclusion, the utilization of NaCl solution does not influence the individual processes occurring during operation. The slight differences in the operated cells shown (see Fig. S1b) are not due to the utilization of NaCl solution but in the authors' opinion to the comparison of individually produced cells and slight differences in the operating conditions such as minimal

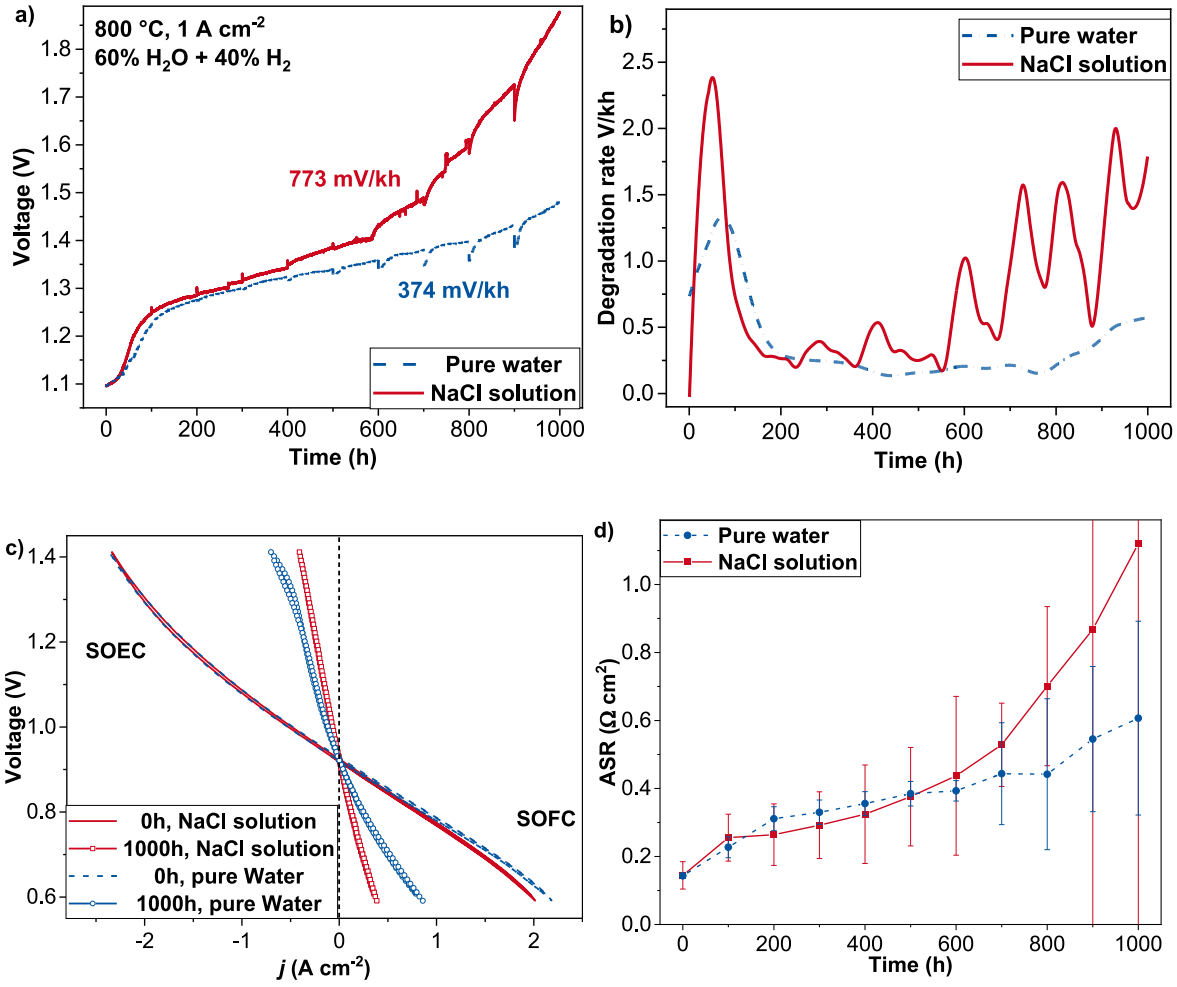

Fig. 2. a) Cell voltage evolution under galvanostatic stability test with 1 A•cm^{-2} in 60 % H_2O and 40 % H_2 at 800 °C and b) corresponding degradation rate as a function of operation time for the utilization of NaCl solution and pure water for steam generation. Corresponding comparison of c) iV curves before and after the stability test and d) the evolution of the ASR as a function of operation time.

temperature variations.

3.2. Long term degradation

3.2.1. Electrochemical performance analysis

In Fig. 2a the voltage development in a long-term stability test with a constant load of −1 A•cm^{-2} with a gas composition of 60 % H_2O + 40 % H_2 utilized from pure and NaCl saturated water at 800 °C is displayed. In Fig. 2b the degradation rate as a function of operating time is plotted. Every 100 h the stability test was interrupted to measure iV curves and EIS. In the case of the utilization of pure water, the voltage increases steeply in the first 200 h from 1.10 V to 1.27 V. After the voltage increases linearly in a time frame from 200 to 800 h from 1.27 V to 1.39 V. After around 800 h of operation time the slope of the curve is slightly increasing, and the voltage increases from 1.39 V to 1.48 V at 1000 h. The same trend was observed before in literature from our and other workgroups for pure water measurements [29,34,35]. In the case of the utilization of saturated NaCl solution, the voltage increases steeply in the first 200 h from 1.10 V to 1.28 V like the pure water measurement. From 200 h to 400 h a linear increase in voltage is observed from 1.28 V to 1.34 V. From 400 h onwards an approximately exponential increase of the voltage is observed from 1.34 V to 1.87 V. Comparing both curves no significant differences in voltage evolution are observed in the first 400 h. After 400 h the voltage of the NaCl operated cell is increasing faster to higher voltages compared to the pure water cell.

This trend is corresponding to the degradation rate evolution shown in Fig. 2b. The absolute numbers of the degradation rate every 100 h were calculated by subtracting the starting voltage from the end voltage and interpolating it to 1000 h. The calculated values are shown in Table 1. From 0 h to 100 h degradation rates over 1000 mV•kh^{-1} are observed for both cells. From 100 to 400 h degradation rates around 250 mV•kh^{-1} are measured. In the case of the saturated NaCl cell, the degradation rate increases from 400 h onwards from around 400 mV•kh^{-1} to values over 1000 mV•kh^{-1} for the time frame 700–1000 h of operation time. Utilizing pure water steady degradation rates of around 200 mV•kh^{-1} are observed from 400 to 800 h of operation. From 800 to 1000 h, an increase in degradation rate is observed reaching 528 mV•kh^{-1} in the time frame from 900 to 1000 h. Therefore, the total degradation rate of the saturated NaCl operated cell is with a value of 773 mV•kh^{-1} higher than for the pure water cell with a value of 374 mV•kh^{-1}. Thus, it seems that the utilization of saturated NaCl solution for the generation of steam has no significant influence in the first 400 h of operation. However, after 400 h an increased degradation rate is observed by using saturated NaCl solution compared to pure water. Thus, the authors expect that this sudden increase in voltage after 400 h is connected to an operation time dependent influence similar to poisoning of an SOEC by HCl reported previously [36]. In this regard, studies on seawater electrolysis did not report an accelerated degradation after 400 h of operation [21,22,27]. This highlights that a higher concentration of sodium chloride is likely responsible for the increase in degradation after 400 h. Based on previous literature studies with a similar used bubbler setup a transported amount of around 15 mg NaCl for 1000 h of operation using a saturated NaCl solution is calculated [27,37]. This is around ten times higher compared to the utilization of seawater in the same operation time. Thus, the test here could be used as an accelerated degradation test for seawater electrolysis in SOECs. Furthermore, negative effects of seawater electrolysis in SOECs could occur after longer operation times of several thousand hours which are not investigated in the referred studies.

Table 1
Overview of the degradation rate in absolute numbers in steps of 100 h of operation time for the utilization of NaCl solution and pure water for steam generation.

Degradation time (h)	Degradation rate (mV•kh^{-1})	
	Pure Water	NaCl solution
0–100	1120	1483
100–200	612	380
200–300	259	280
300–400	217	300
400–500	145	420
500–600	178	490
600–700	200	540
700–800	179	1220
800–900	311	1150
900–1000	528	1510

The cell performance was analysed by AC and DC measurements. In Fig. 2c the iV curves before and after the stability test are plotted. The initial performance of the compared cells operated in pure and NaCl saturated water is identical and reaches 2.33 A•cm^{-2} at 1.4 V and 800 °C in a gas composition of 60 % H_2O + 40 % H_2. The performance decreases significantly after 1000 h for both cells. The current density of the NaCl operated cell and the pure water cell decreases to 0.41 A•cm^{-2} and 0.67 A•cm^{-2} at 1.4 V, respectively. Therefore, the pure water cell's performance decreases by 71 % from the initial performance value which is similar to values reported by our group before [29]. The performance of the saturated NaCl cell decreases by 82 % from the initial performance which again shows the negative impact of the utilization of highly concentrated NaCl solution for SOEC operation. For further investigation, the area specific resistance (ASR) at OCV calculated from impedance measurements is plotted in Fig. 2d as a function of operation time.

The initial ASR value of both cells is similar at a value of 0.145 Ω•cm^2. A sharp increase in ASR in the first 200 h is observed. In the case of the pure water cell, the ASR is steadily increasing linearly for the whole operation time to a maximum value of 0.61 Ω•cm^2 after 1000 h of operation at 800 °C and OCV. The increase between 800 and 1000 h shows a higher slope compared to the time frame from 200 to 800 h. For the NaCl operated cell, an exponential increase in the ASR is seen from 200 to 1000 h. Moreover, the ASR value of the NaCl operated cell exceeds the value of the pure water cell at 500 h reaching a maximum of 1.13 Ω•cm^2 after 1000 h of operation at 800 °C and OCV.

3.2.2. Electrochemical impedance analysis

Next, the impedance data that was recorded at OCV from 0 h to 1000 h in 100 h steps during the stability measurement is further evaluated. In Fig. 3a and b, the Nyquist plots for the NaCl operated cell and the pure water operated cell are shown, respectively. From the plots, it is observed that in the first 200 h, the high frequency intercept with the real impedance axis is not significantly influenced for both cells. After around 200 h of operation, a clear increase in value for the high frequency intercept is observed in the case of both cells. However, the increase is more pronounced in the case of the NaCl operated cell. The origin of this increase is further evaluated later in the manuscript. The low frequency intercept is increasing for both cells over the whole operation window. It is observed that the total increase is more pronounced for the NaCl operated cell compared to the pure water one.

For further insights and deconvolution of the impedance data, the data was fitted to an equivalent circuit model (ECM). The number of circuit elements was estimated using the distribution of relaxation time (DRT) method as shown in Fig. 4a for the cell before the stability test at 800 °C, OCV and 60 % H_2O + 40 % H_2. The DRT suggests four relaxation processes as four distinct peaks are visible labelled P_1 to P_4 as shown in Fig. 4a. The used ECM consists of an inductance in series with a resistor and four RQ elements. The inductance represents the inductive wire effect, and the serial resistor is the ohmic resistance. The error (chi-square) between the collected data and the fit was in the order of magnitude 10^{-7}. Additionally, in Fig. 4c the relative residuals are shown. Fig. 4b shows the individual contribution to the Nyquist plot from the fit. To identify if the fit can describe the altered cell the same procedure was done for every measurement. For representative purposes, the comparative analysis of the experimental data and the fit is shown in Fig. S2 after 700 h of stability test in the supporting

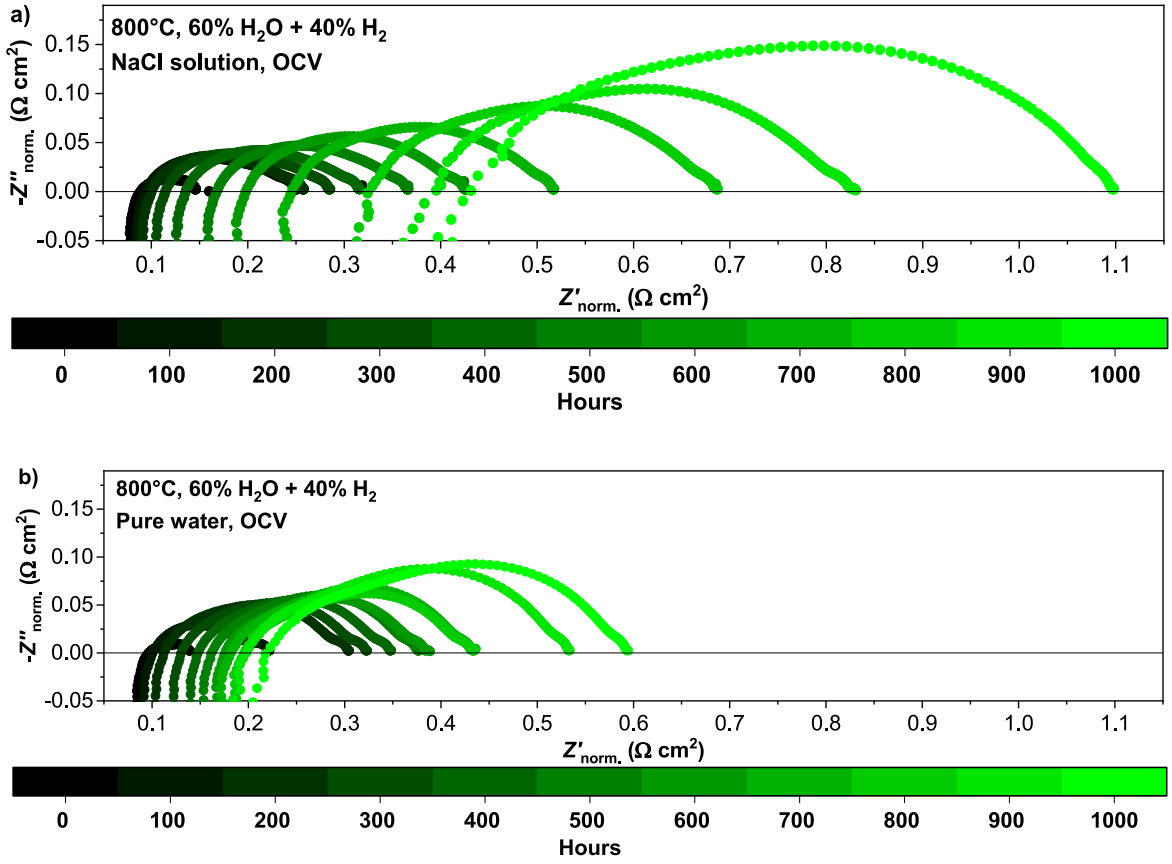

Fig. 3. Nyquist plots as a function of operation time for the utilization of (a) NaCl solution and (b) pure water recorded at 800 °C and OCV with a gas composition of 60 % H_2O + 40 % H_2.

information.

For further investigations, the polarisation resistance and ohmic resistance in dependency on the operation time are plotted in Fig. 5 for the NaCl operated cell in comparison with the pure water cell. In the case of the pure water cell, a clear increase in R_p is observed in the first 200 h of operation from 0.066 Ω•cm^2 to 0.213 Ω•cm^2 whereas the ohmic resistance (R_Ω) is slightly increasing from 0.080 Ω•cm^2 to 0.096 Ω•cm^2. After 200 h until 600 h, the R_p stays at a constant value and the ohmic resistance slightly increases to 0.161 Ω•cm^2. After 600 h the Rp increases reaching a value of 0.464 Ω•cm^2 at 1000 h. The ohmic resistance stays constant from 600 to 1000 h of operation. In the case of the NaCl operated cell, a similar trend is observed in the first 200 h. The R_p increases in the first 200 h from 0.073 Ω•cm^2 to 0.180 Ω•cm^2 whereas the ohmic resistance increases only slightly from 0.078 Ω•cm^2 to 0.086 Ω•cm^2. After 200 h the R_p and R_Ω are increasing exponentially. Comparing the evolution between the pure water and NaCl shows a similar trend including an initial steep increase, a period of small/no increase and a period of steep increase is observed. The last period is more pronounced in the case of the NaCl cell which can be seen as after 700 h the values of R_p surpass the one for the pure water cell. In the case of the R_Ω, a similar trend can be observed until 600 h of the measurement. After 600 h the R_Ω of the NaCl cell increases whereas in the case of the pure water cell, it stays constant. From the trend, it seems that both the R_Ω and R_p are responsible for the accelerated degradation of the NaCl cell. However, the R_p shows the same trend compared to the pure water cell with higher resistance values. The R_Ω of the NaCl operated cell differs in its evolution and value from the pure water cell after 600 h of operation.

Next, the polarisation resistance contributions are investigated in more detail to gather insights about the degradation processes. In Fig. 6a the DRT evolution dependent on the operation time is shown for the cell operated in NaCl solution. From the DRT the low frequency peak P_4 is not significantly changing in magnitude or relaxation frequency. P_3 is slightly increasing in magnitude, P_2 is increasing more pronounced in magnitude than P_3. The high frequency peak P_1 is increasing in magnitude and its relaxation frequency stays constant.

Furthermore, P_2 and P_1 are increasing significantly in magnitude during the first 100 h of operation. After 100 h until 500 h P_1 and P_2 are increasing only slightly whereas after 500 h a significant increase in magnitude is observed. For comparison reasons, the DRT spectra of the pure water cell are shown in Fig. 6b with the same axis scale. In the first 500 h of the measurement, a similar trend for the individual peaks is observed. After 500 h the direct comparison reveals that P_4 is not significantly influenced in magnitude or relaxation frequency using NaCl solution. P_3 similarly increases for both waters. P_2 increases in magnitude more significantly in the case of the NaCl solution. P_1 is increasing more pronounced in magnitude for the NaCl solution compared to the pure water measurement. Thus, from the DRT analysis P_1 and P_2 are the main contributors to the increase in R_p over the whole stability test for both operated cells. However, in the case of the NaCl solution P_2 and P_1 are the major drivers for the higher polarisation resistance increase in comparison with the pure water measurement.

A similar trend can be observed considering the results from the ECM fitting shown in Fig. 6c–d for the NaCl solution and the pure water operation, respectively. The resistance of the low frequency RQ_4 element shows no significant increase in resistance values over the operation window in the case of both cells. The R_{RQ3} shows a slight increase in value over the operation window for both cells. The resistance R_{RQ2} is increasing sharply in the first 200 h of operation for both cells. After 200 h R_{RQ2} is steadily increasing in value whereas a more

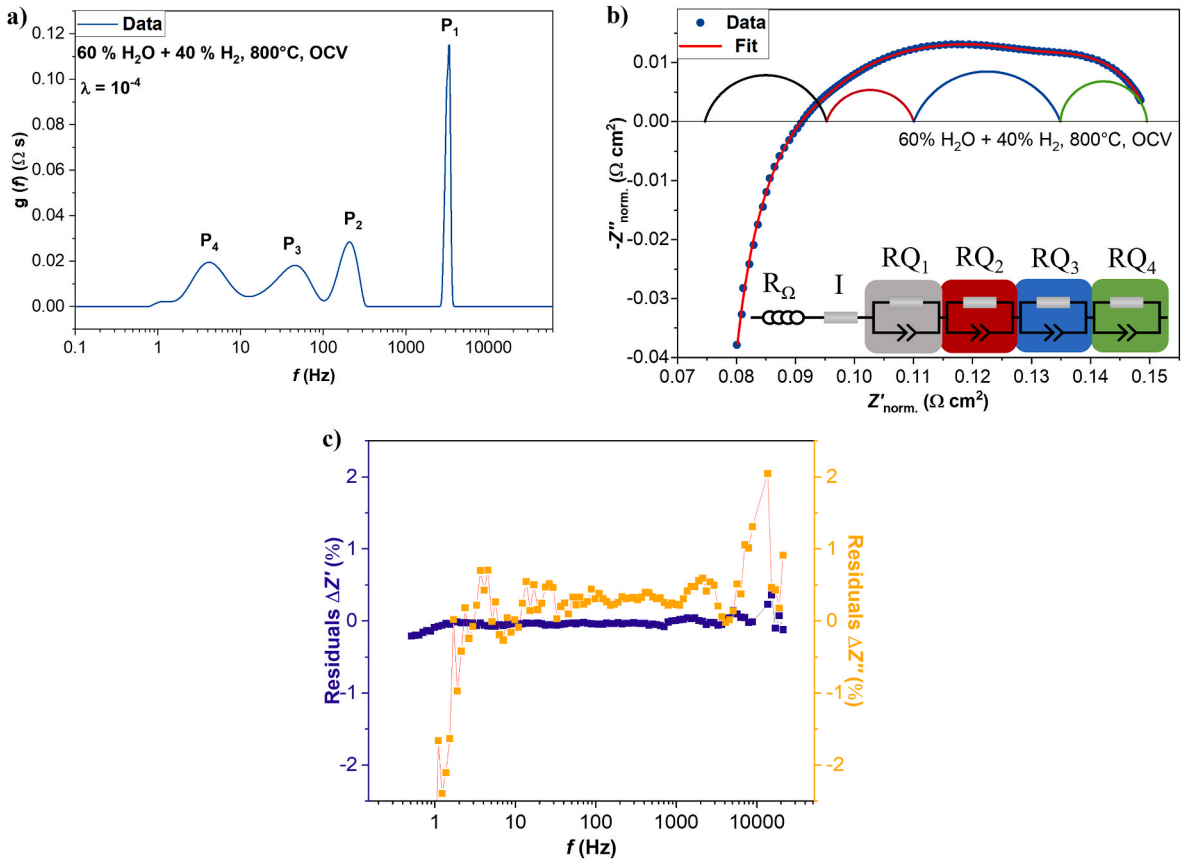

Fig. 4. a) DRT plots of measured data, b) comparison of Nyquist plot of measured and fitted data with the individual contribution of the 4 RQ ECM model and c) relative residuals of the ECM fit in a gas composition of 60 % H_2O+40 % H_2 at 800 °C and OCV.

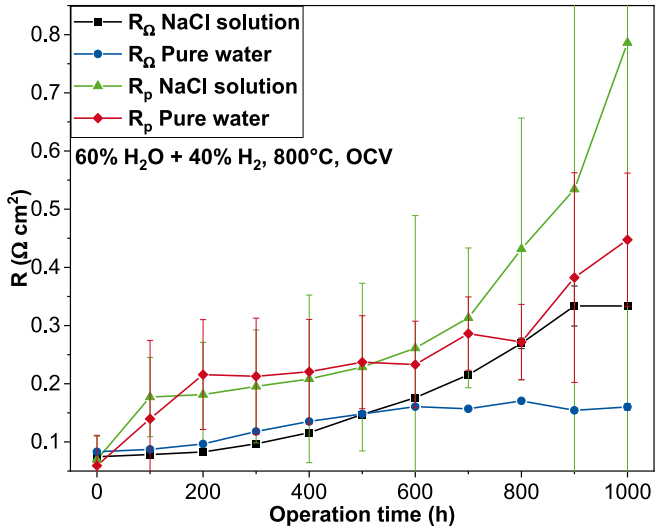

Fig. 5. Evolution of the ohmic and polarisation resistance during the stability test comparing the utilization of steam produced from pure water and NaCl solution. The values are derived from the EIS measurements in a gas composition of 60 % H_2O + 40 % H_2 at 800 °C and OCV.

pronounced increase is noticed for the NaCl solution operated cell. The resistance R_{RQ1} is increasing in the first 200 h for both cells. After 200 h R_{RQ1} stays constant until 400 h and 600 h of operation for the NaCl solution cell and the pure water cell, respectively. After the constant period, a sharp increase in value is observed for both cells. The increase in R_{RQ1} is more pronounced for the NaCl solution operated cell even surpassing the resistance R_{RQ2} in value which is not observed in the case of the pure water cell. From the trend, it is concluded that R_{RQ2} is mainly responsible for the sharp increase in polarisation resistance in the first 200 h of the stability test. R_{RQ1} is mainly responsible for the increase after 500 h of operation in both cells. Furthermore, R_{RQ3} and R_{RQ4} are not significantly contributing to the increase in polarisation resistance. The more pronounced increase in R_p for the NaCl solution operated cell is mainly due to a higher increase in R_{RQ1} whereas R_{RQ2} is increasing more pronounced as well compared to the pure water cell. By considering literature studies and previous results from our working group on Ni-YSZ based fuel electrode supported SOCs the RQ elements are assigned to physical processes. In previous studies, the low frequency process RQ_4 (1–10 Hz) in Ni-YSZ/8YSZ/GDC/LSC cells was associated with gas diffusion processes at the fuel electrode due to its low activation energy and its dependency on the fuel gas content [38–41].

The process associated with RQ_3 (80–500 Hz) in the intermediate frequency region is thermally activated and has been observed to be dependent on a change in oxygen content at the air side and a variation of steam content at the fuel electrode for Ni-YSZ fuel electrode single cells [38,39]. The same trend was observed by an earlier work of our group in this study used cells in steam electrolysis conditions [29]. Furthermore, it was reported to exhibit Arrhenius behaviour [29,42]. Therefore, it is associated with an electrochemical process at the TPBs of the LSC/GDC electrode and an oxygen electrode transport process for its air electrode contribution [38,39]. The fuel electrode contribution is related to a fuel electrode transport process and is reported to dominate the processes between 100 and 500 Hz [38]. The thermally activated processes P_1 (2–10 kHz) and P_2 (0.1–1 kHz) are reported to be attributed as coupled high-frequency processes of a charge transfer at the TPB at the fuel side and the oxide ion transport in the YSZ matrix, respectively [40,41]. It can be concluded that the coupled oxide ion transport and

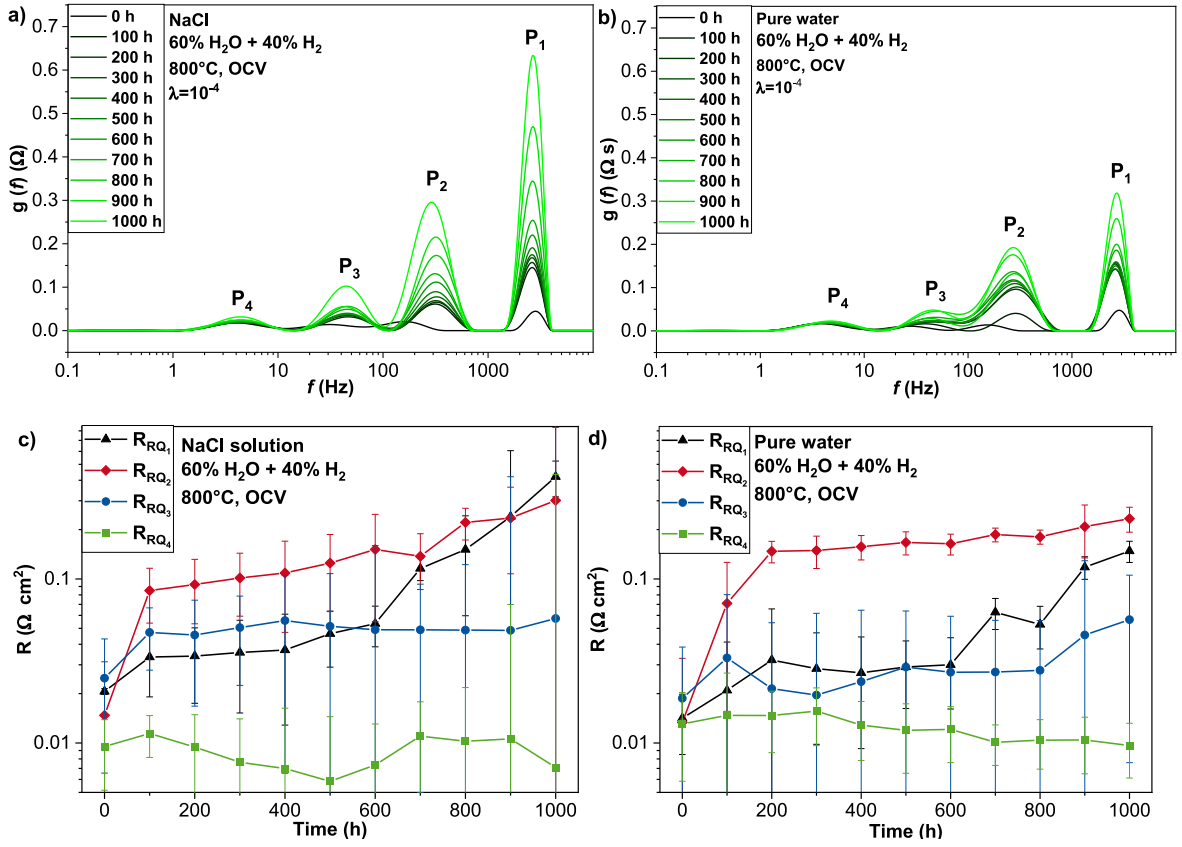

Fig. 6. DRT plots as a function of operation time for a) utilizing steam from NaCl solution and b) utilizing steam from pure water. Individual resistance analysis derived from ECM fitting for c) NaCl solution and d) pure water. Data is derived from EIS measurements at 800 °C and OCV with a gas composition of 60 % H_2O + 40 % H_2.

charge transfer in the Ni-YSZ fuel electrode are mainly responsible for the polarisation degradation of the cell. The more pronounced increase in R_p for the utilizing of NaCl solution compared with pure water is mainly due to an increase in the high frequency charge transfer resistance (P_1) at the TPB in the Ni-YSZ fuel electrode. The higher total resistance is therefore mainly due to an increase of the high frequency coupled charge transfer resistance with oxide ion transport in the Ni-YSZ fuel electrode and the ohmic resistance in the case of NaCl solution operation.

3.3. Post test characterization

3.3.1. Ni-YSZ fuel electrode surface characterization

The differences in degradation behaviour were investigated by post characterization techniques. In the first step, XRD spectra of the surface of the Ni-YSZ electrode were recorded to detect possible salt crystal structures on the surface of the cell. As shown in Fig. S3a in the supporting information no other crystal structures than Ni and YSZ were detected by XRD. Furthermore, no significant differences between the pure water cell and the NaCl operated cell can be distinguished. In the following GI-XRD was performed for the enhanced detection of thin films or impurities on the Ni-YSZ fuel electrode surface. The spectra shown in Fig. S3b in the supporting information show no additional crystal structure in the case of the NaCl operated cell which thus suggests no detectable salt species on the surface of the Ni-YSZ electrode. For an even further enhanced limit of detection XPS measurements were performed for the NaCl operated cell on the surface of the Ni-YSZ electrode. The XPS spectrum for the NaCl operated cell is shown in Fig. 7a. Here peaks at binding energies of 1080 eV and 500 eV are observed referring to Na 1s and Na KLL. Thus, with XPS a Na species can be confirmed on the surface of the NaCl operated cell at an amount of 2.4 at.%. As a reference, the pure water cells XPS spectrum is shown in Fig. S4 in the supporting information.

For further insights, low voltage SEM images and EDX analysis of the Ni-YSZ surface were conducted as shown in Fig. 7b. The authors want to note here that the surface is mostly covered by a Ni contact layer on top of the Ni-YSZ structure. The secondary electron images (SE) show some deposited particles on the surface of the Ni contact layer. In the BSE image, the particles are identified as black whereas the Ni surface is dark grey. With EDX analysis the particles are identified containing sodium as an element. Interestingly, the EDX analysis showed no chlorine detection in the spots where the Na species was found, however, oxygen and carbon were detected. Thus, the authors suggest that the species found in post characterization is sodium carbonate or sodium hydrogen carbonate. Furthermore, the authors noticed during the SEM imaging that the Na species is mainly found on “hills” in the Ni contact layer. In flat places, only a few or no sodium particles are found (see Fig. S5 in the supporting information). Thus, the Na species are not homogeneously distributed on the surface of the Ni contact layer. This could be explained by the deposition on non-contacted areas due to the application of a Ni mesh as a current collector. However, the authors cannot exclude the possibility that the deposition of salt particles is negatively affecting the contact with the current collector which could explain the accelerated increase in ohmic resistance for the NaCl operated cell. The salt deposition mechanism and the formation of a sodium carbonate species are not clear yet. The authors propose the following deposition mechanisms which explain the detection of a sodium carbonate species. Firstly, NaCl particles are transported to the cell via aerosols [43]. During operation, the degradation mechanism via $Ni(OH)_x$ formation in the Ni-YSZ takes place [44]. By the formation of $Ni(OH)_x$ a chlorination mechanism could take place with NaCl as agent resulting in NiCl or $NiCl_2$ and NaOH formation [45]. After $NiCl_2$ is reduced back to Ni by the

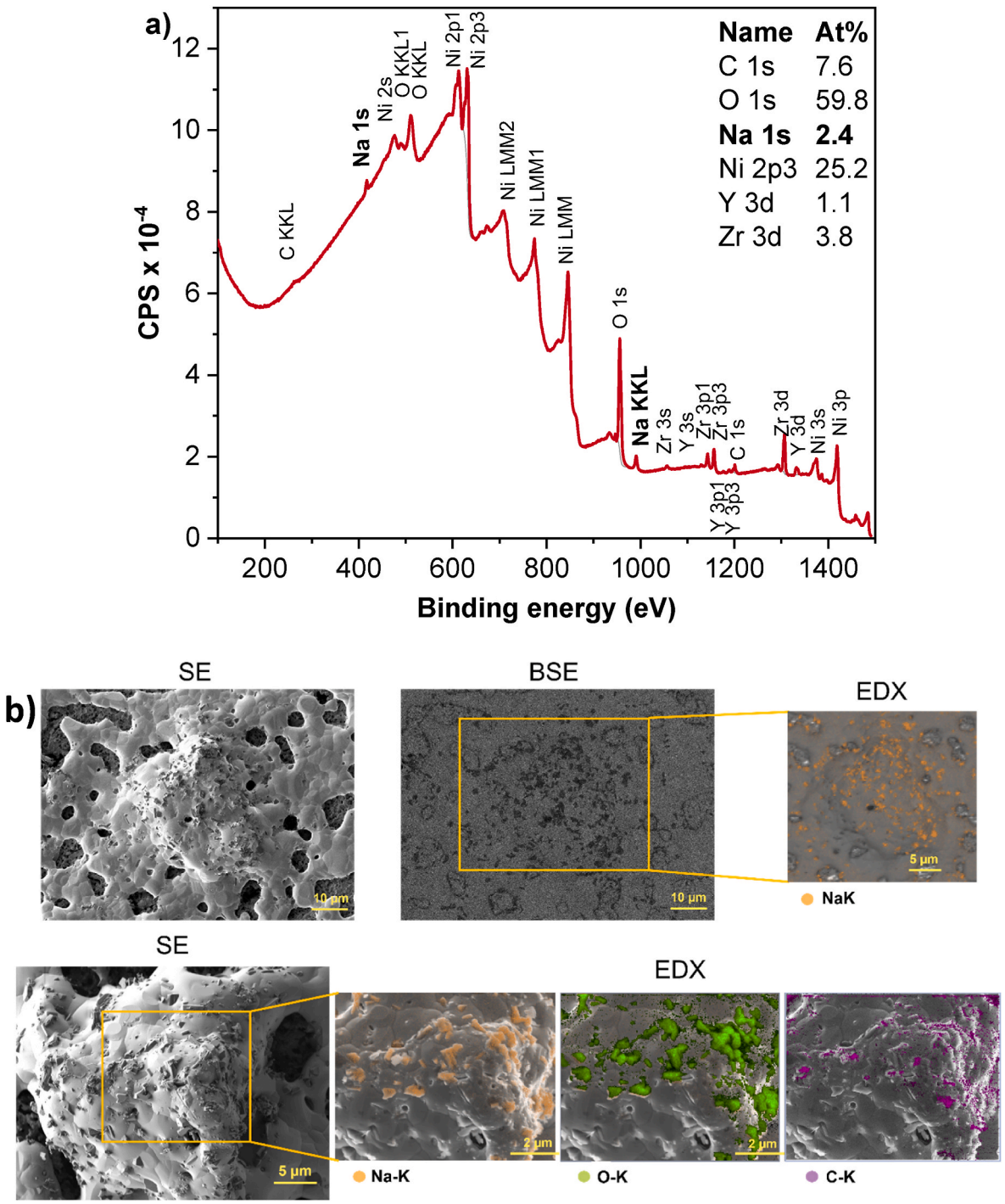

Fig. 7. a) XPS spectrum of the fuel electrode surface of the degraded NaCl solution cell at room temperature. b) SEM images including SE, BSE and EDX maps of the Ni-YSZ fuel electrode surface of the degraded NaCl solution cell.

hydrogen atmosphere under the formation of HCl [46]. In the authors' opinion, a mechanism where HCl is forming is most feasible as it is most thermodynamically stable under the operation conditions [47,48]. Furthermore, studies on the effect of HCl contamination on the degradation of a SOFC reported an increased degradation with a major effect on the charge transfer at the Ni containing fuel electrode which would match with our electrochemical results [48,49]. One study on the effect of 1 ppm HCl in the feed gas of an SOEC system reported a sudden increase in voltage after around 400 h of operation due to a limitation in the charge transfer of the Ni-YSZ fuel electrode which is like our results shown here [50]. By cooling down the cell and exposure to air atmosphere the NaOH is converted to a sodium carbonate species. However, in-operando outlet gas analysis by mass spectroscopy revealed no detection of a chlorine species and no Cl was not found during SEM-EDX analysis. Thus, the deposition mechanism must be investigated further in future.

3.3.2. *Cross section analysis*

The cell operated utilizing saturated sodium chloride was broken in half and the cross section was analysed by SEM. No polishing or FIB cutting was done to not flush out or destroy salt particles that could be present in the cross section of the fuel electrode. In the SE images shown

in Fig. 8a small particles in the nanoscale are observed to be deposited or covering some particles in the functional layer of the Ni-YSZ fuel electrode. Due to the scale of the particles and beam damage issues, it was not possible to identify the composition of the nanoparticles by EDX, however, it was observed that these particles are exclusively found on Ni particles and not on the TPBs between Ni and YSZ particles or on YSZ particles as shown in Fig. S6 in the supporting information. However, in the pure water sample, similar nanoparticles are found in the active functional layer of the Ni/YSZ fuel electrode as shown in Fig. 8a. Thus, the nanoparticles are expected to be ZrO_2 particles as discussed previously in the literature [51,52]. By EDX analysis several spots of the broken cross section were scanned to detect impurities. Here data acquisition was difficult due to sensitivity to beam damage of the cross section. Some of the gathered data suggest the deposition of a Na species in the cross section of the Ni-YSZ fuel electrode. For instance, an exemplary EDX mapping measurement is shown in Fig. 8a in this measurement 0.3 wt% of Na is detected. However, no clear Na containing nanoparticles in the μm range are found in the cross section by the mapping. Other measurements show similar results which are shown in Fig. S7 in the supporting information. The results suggest that salt is transported into the porous Ni-YSZ fuel electrode and deposited into the porous microstructure. In literature, a study investigated the salt particle production by bubble bursting which is like our bubbler system to produce steam. Here the diameter of the transported salt by bubbling through NaCl solution is reported to be between 10 and 100 nm [37]. Thus, a deposition of small hard-to-detect salt particles is feasible.

It must be mentioned that no delamination of the fuel or air electrode was observed in the cells as shown in Fig. S8a in the supporting information. Therefore, an accelerated increase in polarisation or ohmic resistance caused by delamination of the oxygen side as described in the literature, can be excluded [53]. From the SEM images of the polished cross sections similar microstructures of the air electrode are observed for the NaCl and pure water operated cell as shown in Fig. S8b. Thus, a significant contribution of the oxygen electrode by for example different quality of the electrodes in both operated cells is unlikely.

Next, the embedded and polished cross sections of the operated cells are investigated. Fig. 8b shows the Ni-YSZ fuel electrode cross section of a reduced cell compared to the 1000 h operated cells in pure water and saturated NaCl solution. At the top of the pictures, the BSE images of the polished cross section of the fuel electrode are shown. The brighter particles refer to Ni whereas the darker particles to the YSZ phase. Below the respective EDX maps of the Ni phase and Zr phase are shown. In the reduced cell, small and homogeneously distributed Ni particles in the active functional layer of the Ni-YSZ fuel electrode are observed. In the case of the pure water degraded cell, an agglomeration of Ni particles in the functional layer of the Ni-YSZ fuel electrode as well as in the support layer is observed. In the saturated NaCl solution operated cell an even higher agglomeration of Ni particles is visible. Furthermore, a coarsening of the YSZ phase is observed in the degraded cells compared to the reduced cells. Here again, the coarsening is more present in the NaCl operated cell. A quantitative analysis of the SEM/EDS images is shown in Table 2. A higher Ni fraction in the NaCl operated cell is observed for the 10 μm thick active layer directly above the electrolyte compared to the pure water cell. Thus, in the pure water cell a depletion of Ni away from the electrolyte/electrode interface takes place which is quantitatively not observed for the NaCl operated cell. However, a higher average Ni and Zr particle size in the active layer is observed for the NaCl operated cell compared to the pure water operated cell and the pristine one. Thus, a higher Ni agglomeration is observed in the case of the NaCl operated cell compared to the pure water cell. From the post characterization results and the electrochemical results, it is concluded that a more pronounced decrease in TPB length in the Ni-YSZ fuel electrode is observed for the NaCl operated cell compared to the pure water cell due to the higher particle sizes of both Ni and Zr leading to a higher degradation rate.

As discussed above different microstructural evolutions are observed for the NaCl and pure water operated cells. Thus, the question arises of how the impurities of NaCl in the steam influence the degradation mechanism such that higher Ni agglomeration and no Ni depletion in the active layer of the Ni-YSZ electrode is observed for the NaCl operated cell. Interestingly, different studies with chlorine containing impurities in the feed gas of SOCs reported microstructural changes in the active Ni containing layer of the fuel electrode [54–56]. Taking into account the proposed deposition mechanism and the formation of HCl (see section 3.3.1), one hypothesis is the blocking of active reaction sites (triple phase boundaries) by chlorine adsorption [48] or salt deposition in the Ni-YSZ fuel electrode active functional layer. This increases the effective local overpotential at the remaining active sites and could cause higher Ni agglomeration and migration during operation, decreasing the TPB length and therefore leading to higher operating voltages. Another possibility is the influence of the formation of $NiCl_2$ and its consecutive reduction which was described earlier in the manuscript. The results hint towards a time dependent degradation by the transport of NaCl to the cell. However, as said these phenomena should be investigated by detailed transportation experiments in future work.

4. Conclusion

The usage of sodium chloride concentrated solution was evaluated in SOEC Ni-YSZ fuel electrode based commercial single cell water electrolysis to evaluate the utilization of high saline wastewaters from the industry. In addition, the results could provide a prediction for the usage of seawater in SOECs. It was observed that the initial performance and processes are not influenced by steam generated from concentrated sodium chloride solution.

However, it was observed that the stability of an electrolysis operation is negatively influenced by the utilization of sodium chloride solution compared to pure water operation. The increase in degradation is visible after 400 h of operation and is due to an accelerated increase in ohmic and polarisation resistance. More specifically, the increase in polarisation resistance mainly corresponds to an increase in charge transfer resistance at the Ni-YSZ fuel electrode.

Post-test characterization of the surface of the Ni-YSZ fuel electrode showed an inhomogeneous deposited sodium species that was identified as sodium carbonate or sodium hydrogen carbonate with particle sizes of around 500 nm. Furthermore, small nanoparticles with sizes around 5–50 nm were found in the Ni-YSZ fuel electrode. The nanoparticles were suggested to be ZrO_2 which is exclusively deposited on Ni particles in the functional layer of the Ni-YSZ fuel electrode. EDX analysis of the Ni-YSZ suggests the transport and deposition of salt particles in the Ni-YSZ fuel electrode. In addition, SEM and EDX analysis of the polished cross section showed that accelerated Ni agglomeration is observed in the NaCl operated cell decreasing the TPB length.

The results found in the study suggest that high saline waters are not suitable for their direct utilization for steam generation in SOECs. Furthermore, direct operation with salt containing waters such as seawater should be handled with care as effects on the stability of the SOECs could be observed only after long degradation times. In further studies, it should be evaluated if the negative effects on the SOEC stability could be reversed in situ by adjusting the operating temperature or switching to SOFC mode and consecutive flushing out the deposited particles or adsorbed impurities.

CRediT authorship contribution statement

Jan Uecker: Writing – review & editing, Writing – original draft, Visualization, Validation, Methodology, Investigation, Formal analysis, Data curation, Conceptualization. **Lucy Nohl:** Visualization, Validation, Supervision, Methodology, Conceptualization. **Vaibhav Vibhu:** Writing – review & editing, Visualization, Validation, Supervision, Methodology, Conceptualization. **Jean-Pierre Poc:** Writing – review & editing, Methodology. **Pritam Chakraborty:** Writing – review & editing,

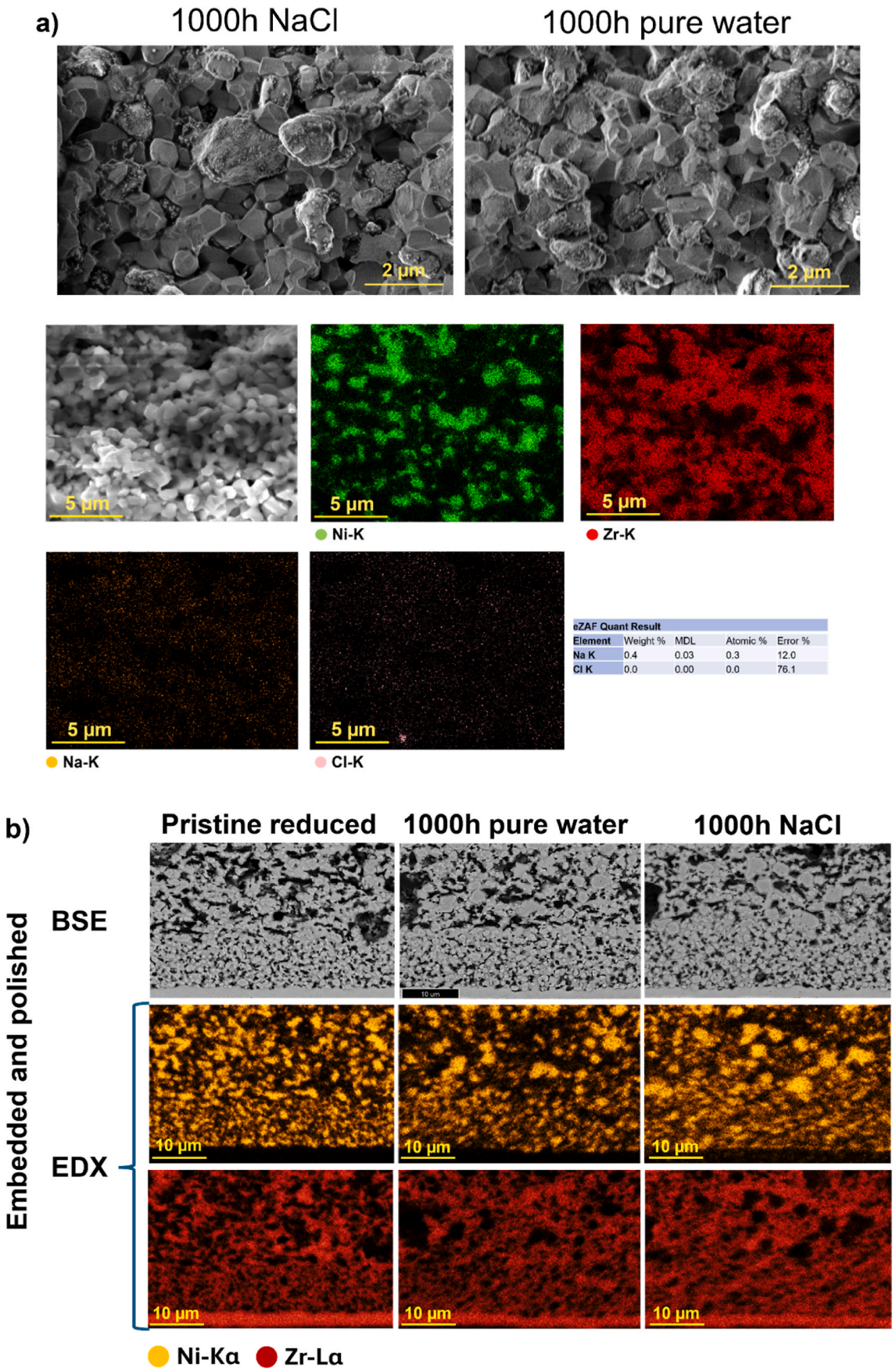

Fig. 8. a) Cross-section SE images of both cells and EDX mapping of the Ni-YSZ fuel electrode of the NaCl operated cell and b) polished cross-sections of both cells.

Table 2
Quantitative analysis using the SEM/EDX images for the active functional layer and support layer of the Ni-YSZ fuel electrode.

Fraction	Pristine active layer	Pristine support layer	Pure water active layer	Pure water support layer	NaCl active layer	NaCl support layer
Porosity	28 %	39 %	27 %	33 %	28 %	32 %
Ni fraction	30 %	27 %	26 %	23 %	29 %	25 %
Zr fraction	42 %	34 %	46 %	44 %	43 %	43 %
Average Ni particle size	0.97 μm	1.09 μm	1.04 μm	1.01 μm	1.11 μm	1.11 μm
Average Zr particle size	1.12 μm	1.39 μm	1.23 μm	1.65 μm	1.36 μm	1.67 μm

Methodology. **Izaak C. Vinke:** Visualization, Validation, Supervision, Project administration, Methodology, Conceptualization. **Shibabrata Basak:** Visualization, Validation, Supervision. **L.G.J.(Bert) de Haart:** Visualization, Validation, Supervision, Project administration, Methodology, Conceptualization. **Rüdiger-A. Eichel:** Supervision, Project administration.

Declaration of competing interest

The authors declare that they have no known competing financial interests or personal relationships that could have appeared to influence the work reported in this paper.

Acknowledgments

The authors gratefully acknowledge funding by the *German Federal Ministry of Education and Research* (BMBF) within the PRELUDE Project under grant agreement number 03SF0650A.

Appendix A. Supplementary data

Supplementary data to this article can be found online at https://doi.org/10.1016/j.jpowsour.2025.236390.

Data availability

Data will be made available on request.

References

[1] S.a.C.O. United Nations Educational, The United Nations World Water Development Report 2023: partnerships and cooperation for water, Place de Fontenoy, 75352 Paris 07 SP, 2023. France.
[2] P. Burek, Y. Satoh, G.W. Fischer, M.T. Kahil, A. Scherzer, S. Tramberend, L.F. Nava, Y. Wada, S. Eisner, M. Flörke, N. Hanasaki, P. Magnuszewski, B. Cosgrove, D. Wiberg, Water Futures and Solution - Fast Track Initiative (Final Report), 2016.
[3] C. He, Z. Liu, J. Wu, X. Pan, Z. Fang, J. Li, B.A. Bryan, Future global urban water scarcity and potential solutions, Nat. Commun. 12 (2021) 4667.
[4] W. Bank, High and Dry: Climate Change, Water, and the Economy, The World Bank, 2016.
[5] B. Clarke, F. Otto, R. Stuart-Smith, L. Harrington, Extreme weather impacts of climate change: an attribution perspective, Environ. Res.: Climate 1 (2022) 012001.
[6] Impacts of 1.5°C global warming on natural and human systems, in: C. Intergovernmental Panel on Climate (Ed.), Global Warming of 1.5°C: IPCC Special Report on Impacts of Global Warming of 1.5°C above Pre-industrial Levels in Context of Strengthening Response to Climate Change, Sustainable Development, and Efforts to Eradicate Poverty, Cambridge University Press, Cambridge, 2022, pp. 175–312.
[7] M.B. Mogensen, M. Chen, H.L. Frandsen, C. Graves, J.B. Hansen, K.V. Hansen, A. Hauch, T. Jacobsen, S.H. Jensen, T.L. Skafte, X. Sun, Reversible solid-oxide cells for clean and sustainable energy, Clean Energy 3 (2019) 175–201.
[8] R. Geres, A. Kohn, S. Lenz, F. Ausfelder, A.M. Bazzanella, A. Möller, Roadmap CHemie 2050. Auf dem Weg zu euner traibhausgasneutralen chemischen Industrie in Deutschland, DECHEMA, 2019. https://www.vci.de/vci/downloads-vci/publikation/2019-10-09-studie-roadmap-chemie-2050-treibhausgasneutralitaet.pdf.
[9] S. Lechtenböhmer, S. Samadi, A. Leipprand, C. Schneider, Grüner Wasserstoff, das dritte Standbein der Energiewende?, 2019.
[10] J. Schleich, T. Hillenbrand, Determinants of residential water demand in Germany, Ecol. Econ. 68 (2009) 1756–1769.
[11] W.B. Group, Global solar atlas 2.0. https://globalsolaratlas.info, 2024.
[12] I.S. Al-Mutaz, Environmental impact of seawater desalination plants, Environ. Monit. Assess. 16 (1991) 75–84.
[13] S. Lattemann, T. Höpner, Environmental impact and impact assessment of seawater desalination, Desalination 220 (2008) 1–15.
[14] I. Ihsanullah, M.A. Atieh, M. Sajid, M.K. Nazal, Desalination and environment: a critical analysis of impacts, mitigation strategies, and greener desalination technologies, Sci. Total Environ. 780 (2021) 146585.
[15] G.A. Tularam, M. Ilahee, Environmental concerns of desalinating seawater using reverse osmosis, J. Environ. Monit. 9 (2007) 805–813.
[16] L. Yu, Q. Zhu, S. Song, B. McElhenny, D. Wang, C. Wu, Z. Qin, J. Bao, Y. Yu, S. Chen, Z. Ren, Non-noble metal-nitride based electrocatalysts for high-performance alkaline seawater electrolysis, Nat. Commun. 10 (2019) 5106.
[17] J. Guo, Y. Zheng, Z. Hu, C. Zheng, J. Mao, K. Du, M. Jaroniec, S.-Z. Qiao, T. Ling, Direct seawater electrolysis by adjusting the local reaction environment of a catalyst, Nat. Energy 8 (2023) 264–272.
[18] H. Xie, Z. Zhao, T. Liu, Y. Wu, C. Lan, W. Jiang, L. Zhu, Y. Wang, D. Yang, Z. Shao, A membrane-based seawater electrolyser for hydrogen generation, Nature 612 (2022) 673–678.
[19] S. Dresp, F. Dionigi, M. Klingenhof, P. Strasser, Direct electrolytic splitting of seawater: opportunities and challenges, ACS Energy Lett. 4 (2019) 933–942.
[20] C.K. Lim, Q. Liu, J. Zhou, Q. Sun, S.H. Chan, High-temperature electrolysis of synthetic seawater using solid oxide electrolyzer cells, J. Power Sources 342 (2017) 79–87.
[21] J. Uecker, I.D. Unachukwu, V. Vibhu, I.C. Vinke, L.G.J. de Haart, R.-A. Eichel, Gadolinium doped ceria as nickel–free fuel electrode in high temperature CO2-electrolysis, Chemelectrochem 11 (2024) e202300617.
[22] Z. Liu, B. Han, Y. Zhao, F. Hu, W. Liu, W. Guan, S.C. Singhal, Reversible cycling performance of a flat-tube solid oxide cell for seawater electrolysis, Energy Convers. Manag. 258 (2022) 115543.
[23] A. Krzyżanowska, E. Milchert, M. Bartkowiak, Dehydrochlorination of 1,3-dichloropropan-2-Ol by alcium and sodium hydroxide solutions, Pol. J. Chem. Technol. 16 (2014) 86–90.
[24] P. Ooms, A. Bulan, R. Weber, J. Rechner, M. Traving, Verfahren zur Herstellung von Polycarbonat, Covestro Deutschland AG, 2015.
[25] X. Liu, Z. Zhang, L. Zhang, S. Bu, W. Xu, C. Shi, J. Fang, C. Xu, Separation of sodium sulfate from high-salt wastewater of lead-acid batteries, Chem. Eng. Res. Des. 176 (2021) 194–201.
[26] K.M. Conroy, F. Chen, O.H. Tuovinen, K.M. Mancl, Effect of sodium chloride concentration on removal of chemical oxygen demand and ammonia from Turkey processing wastewater in sand bioreactors, Appl. Eng. Agric. 36 (2020) 33–37.
[27] Z. Liu, B. Han, Z. Lu, W. Guan, Y. Li, C. Song, L. Chen, S.C. Singhal, Efficiency and stability of hydrogen production from seawater using solid oxide electrolysis cells, Appl. Energy 300 (2021) 117439.
[28] H. Pan, A. Wu, S.F. Au, Y. Yang, Z. Song, Z. Liu, X. Gong, W. Guan, Effect of the steam/hydrogen ratio on the performance of flat-tube solid oxide electrolysis cells for seawater, Sustain. Energy Fuels 7 (2023) 3333–3341.
[29] S.E. Wolf, V. Vibhu, E. Tröster, I.C. Vinke, R.-A. Eichel, L.G.J. de Haart, Steam electrolysis vs. Co-electrolysis: mechanistic studies of long-term solid oxide electrolysis cells, Energies 15 (2022) 5449.
[30] K. Schiemann, V. Vibhu, S. Yildiz, I.C. Vinke, R.-A. Eichel, L.G.J. de Haart, Chrome poisoning of non-manganiferous cathode materials in solid oxide fuel cells (SOFCs), ECS Trans. 78 (2017) 1027.
[31] B.A. Boukamp, A. Rolle, Analysis and application of distribution of relaxation times in solid state ionics, Solid State Ionics 302 (2017) 12–18.
[32] S. van der Walt, J.L. Schönberger, J. Nunez-Iglesias, F. Boulogne, J.D. Warner, N. Yager, E. Gouillart, T. Yu, scikit-image: image processing in Python, PeerJ 2 (2014) e453.
[33] S. Foit, L. Dittrich, T. Duyster, I. Vinke, R.-A. Eichel, L.G.J. de Haart, Direct solid oxide electrolysis of carbon dioxide: analysis of performance and processes, Processes 8 (2020) 1390.
[34] X. Sun, P.V. Hendriksen, M.B. Mogensen, M. Chen, Degradation in solid oxide electrolysis cells during long term testing, Fuel Cell. 19 (2019) 740–747.
[35] M.S. Sohal, J.E. O'Brien, C.M. Stoots, V.I. Sharma, B. Yildiz, A. Virkar, Degradation issues in solid oxide cells during high temperature electrolysis, J. Fuel Cell Sci. Technol. 9 (2011).
[36] G. Jeanmonod, S. Diethelm, J. van Herle, Poisoning effects of chlorine on a solid oxide cell operated in co-electrolysis, J. Power Sources 506 (2021) 230247.
[37] L.M. Russell, E.G. Singh, Submicron salt particle production in bubble bursting, Aerosol. Sci. Technol. 40 (2006) 664–671.
[38] P. Caliandro, A. Nakajo, S. Diethelm, J. van Herle, Model-assisted identification of solid oxide cell elementary processes by electrochemical impedance spectroscopy measurements, J. Power Sources 436 (2019) 226838.
[39] A. Leonide, Y. Apel, E. Ivers-Tiffee, SOFC modeling and parameter identification by means of impedance spectroscopy, ECS Trans. 19 (2009) 81.

[40] M. Trini, A. Hauch, S. De Angelis, X. Tong, P.V. Hendriksen, M. Chen, Comparison of microstructural evolution of fuel electrodes in solid oxide fuel cells and electrolysis cells, J. Power Sources 450 (2020) 227599.
[41] V. Sonn, A. Leonide, E. Ivers-Tiffée, Combined deconvolution and CNLS fitting approach applied on the impedance response of technical Ni / 8YSZ cermet electrodes, J. Electrochem. Soc. 155 (2008) B675.
[42] S.E. Wolf, L. Dittrich, M. Nohl, T. Duyster, I.C. Vinke, R.-A. Eichel, L.G.J. de Haart, Boundary investigation of high-temperature Co-electrolysis towards direct CO2 electrolysis, J. Electrochem. Soc. 169 (2022) 034531.
[43] D.M. Murphy, K.D. Froyd, H. Bian, C.A. Brock, J.E. Dibb, J.P. DiGangi, G. Diskin, M. Dollner, A. Kupc, E.M. Scheuer, G.P. Schill, B. Weinzierl, C.J. Williamson, P. Yu, The distribution of sea-salt aerosol in the global troposphere, Atmos. Chem. Phys. 19 (2019) 4093–4104.
[44] M.B. Mogensen, M. Chen, H.L. Frandsen, C. Graves, A. Hauch, P.V. Hendriksen, T. Jacobsen, S.H. Jensen, T.L. Skafte, X. Sun, Ni migration in solid oxide cell electrodes: review and revised hypothesis, Fuel Cell. 21 (2021) 415–429.
[45] S. Zhou, Y. Wei, B. Li, H. Wang, B. Ma, C. Wang, Mechanism of sodium chloride in promoting reduction of high-magnesium low-nickel oxide ore, Sci. Rep. 6 (2016) 29061.
[46] M. Sokić, Ž. Kamberović, V. Nikolić, B. Marković, M. Korać, Z. Anđić, M. Gavrilovski, Kinetics of NiO and NiCl2 hydrogen reduction as precursors and properties of produced Ni/Al2O3 and Ni-Pd/Al2O3 catalysts, Sci. World J. (2015) 601970, 2015.
[47] J. Bao, G.N. Krishnan, P. Jayaweera, J. Perez-Mariano, A. Sanjurjo, Effect of various coal contaminants on the performance of solid oxide fuel cells: Part I. Accelerated testing, J. Power Sources 193 (2009) 607–616.
[48] J.P. Trembly, R.S. Gemmen, D.J. Bayless, The effect of coal syngas containing HCl on the performance of solid oxide fuel cells: investigations into the effect of operational temperature and HCl concentration, J. Power Sources 169 (2007) 347–354.
[49] F.N. Cayan, M. Zhi, S.R. Pakalapati, I. Celik, N. Wu, R. Gemmen, Effects of coal syngas impurities on anodes of solid oxide fuel cells, J. Power Sources 185 (2008) 595–602.
[50] H. Madi, A. Lanzini, D. Papurello, S. Diethelm, C. Ludwig, M. Santarelli, J. Van herle, Solid oxide fuel cell anode degradation by the effect of hydrogen chloride in stack and single cell environments, J. Power Sources 326 (2016) 349–356.
[51] M. Chen, Y.-L. Liu, J.J. Bentzen, W. Zhang, X. Sun, A. Hauch, Y. Tao, J.R. Bowen, P. V. Hendriksen, Microstructural degradation of Ni/YSZ electrodes in solid oxide electrolysis cells under high current, J. Electrochem. Soc. 160 (2013) F883.
[52] F. Tietz, D. Sebold, A. Brisse, J. Schefold, Degradation phenomena in a solid oxide electrolysis cell after 9000 h of operation, J. Power Sources 223 (2013) 129–135.
[53] T. Yang, Y. Fan, J. Liu, H. Finklea, S. Lee, B. Guan, H.W. Abernathy, T.L. Kalapos, G.A. Hackett, Multiphysics modeling of SOFC performance degradation caused by interface delamination and active layer cracking, Int. J. Hydrogen Energy 47 (2022) 41124–41137.
[54] T.S. Li, C. Xu, T. Chen, H. Miao, W.G. Wang, Chlorine contaminants poisoning of solid oxide fuel cells, J. Solid State Electrochem. 15 (2011) 1077–1085.
[55] C. Xu, M. Gong, J.W. Zondlo, X. Liu, H.O. Finklea, The effect of HCl in syngas on Ni–YSZ anode-supported solid oxide fuel cells, J. Power Sources 195 (2010) 2149–2158.
[56] K. Haga, Y. Shiratori, K. Ito, K. Sasaki, Chlorine poisoning of SOFC Ni-cermet anodes, J. Electrochem. Soc. 155 (2008) B1233.